Acta Crystallographica Section B
Structural Science, Crystal Engineering and Materials
ISSN 2052-5206

Solid-state transformation of nanocrystalline phyllomanganate into tectomanganate: influence of initial layer and interlayer structure

Sylvain Grangeon, Bruno Lanson and Martine Lanson

Acta Cryst. (2014). B**70**, 828–838

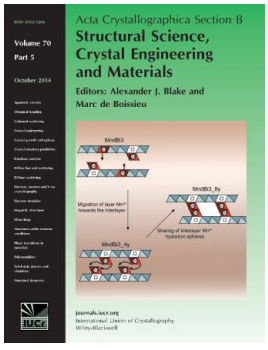

Acta Crystallographica Section B: Structural Science, Crystal Engineering and Materials publishes scientific articles related to the structural science of compounds and materials in the widest sense. Knowledge of the arrangements of atoms, including their temporal variations and dependencies on temperature and pressure, is often the key to understanding physical and chemical phenomena and is crucial for the design of new materials and supramolecular devices. *Acta Crystallographica B* is the forum for the publication of such contributions. Scientific developments based on experimental studies as well as those based on theoretical approaches, including crystal-structure prediction, structure–property relations and the use of databases of crystal structures, are published.

Acta Crystallographica Section B
Structural Science, Crystal Engineering and Materials
ISSN 2052-5206

Solid-state transformation of nanocrystalline phyllomanganate into tectomanganate: influence of initial layer and interlayer structure

Sylvain Grangeon,[a,b]*‡ Bruno Lanson[a,b] and Martine Lanson[a,b]

[a]University of Grenoble Alpes, ISTerre, F-38041 Grenoble, France, and [b]CNRS, ISTerre, F-38041 Grenoble, France

‡ Present address: BRGM, 3 avenue Claude Guillemin, BP36009, 45060 Orléans CEDEX 2, France.

Correspondence e-mail: s.grangeon@brgm.fr

Received 18 March 2014
Accepted 11 June 2014

In surficial environments, the fate of many elements is influenced by their interactions with the phyllomanganate vernadite, a nano-sized and turbostratic variety of birnessite. To advance our understanding of the surface reactivity of vernadite as a function of pH, synthetic vernadite (δ-MnO_2) was equilibrated at pH ranging from 3 to 10 and characterized structurally using chemical methods, thermogravimetry and modelling of powder X-ray diffraction (XRD) patterns. With decreasing pH, the number of vacant layer sites increases in the octahedral layers of δ-MnO_2 (from 0.14 per layer octahedron at pH 10 to 0.17 at pH 3), whereas the number of layer Mn^{3+} is, within errors, equal to 0.12 per layer octahedron over the whole pH range. Vacant layer sites are capped by interlayer Mn^{3+} sorbed as triple corner-sharing surface complexes (TC sites). The increasing number of interlayer Mn^{3+} with decreasing pH (from 0.075 per layer octahedron at pH 10 to 0.175 at pH 3) results in the decrease of the average Mn oxidation degree (from 3.80 ± 0.01 at pH 10 to 3.70 ± 0.01 at pH 3) and in the lowering of the Na/Mn ratio (from 27.66 ± 0.20 at pH 10 to 6.99 ± 0.16 at pH 3). In addition, in-plane unit-cell parameters are negatively correlated to the number of interlayer Mn at TC sites and decrease with decreasing pH (from $b = 2.842$ Å at pH 10 to $b = 2.834$ Å at pH 3), layer symmetry being systematically hexagonal with $a = b \times 3^{1/2}$. Finally, modelling of X-ray diffraction (XRD) patterns indicates that crystallite size in the **ab** plane and along the **c*** axis decreases with decreasing pH, ranging respectively from 7 nm to 6 nm, and from 1.2 nm to 1.0 nm (pH 10 and 3, respectively). Following their characterization, dry samples were sealed in polystyrene vials, kept in the dark, and re-analysed 4 and 8 years later. With ageing time and despite the dry state, layer Mn^{3+} extensively migrates to the interlayer most likely to minimize steric strains resulting from the Jahn–Teller distortion of Mn^{3+} octahedra. When the number of interlayer Mn^{3+} at TC sites resulting from this migration reaches the maximum value of $\sim 1/3$ per layer octahedron, interlayer species from adjacent layers share their coordination sphere, resulting in cryptomelane-like tunnel structure fragments (with a 2×2 tunnel size) with a significantly improved layer stacking order.

1. Introduction

δ-MnO_2 is the synthetic analogue of vernadite and of the three-dimensionally ordered birnessite, two phyllomanganates whose ideal structures consist of layers of $(MnO_6)^{8-}$ octahedra connected through their edges with a layer-to-layer distance of ~ 7.2 Å (Giovanoli, 1980; Chukhrov *et al.*, 1985). Layer stacking is turbostratic both in vernadite and in δ-MnO_2, with the systematic occurrence of random translation and/or rota-

tion between parallel successive layers. To our knowledge, the stoichiometric version of vernadite has not been observed to date owing to two main types of chemical defects: vacant layer sites and substitution of layer Mn^{4+} by cations of lower vacancy (*e.g.* Mn^{3+}). Both types of defects result in a net negative layer charge that is compensated for by the presence of hydrated interlayer cations. These cations typically form outer-sphere complexes in the middle of the interlayer space (*e.g.* Na^{+}, Ca^{2+}) when isomorphic substitutions occur in the layer. Contrastingly, they form inner-sphere complexes above/below layer vacancies (*e.g.* $Mn^{2+/3+}$, metals such as Ni^{2+}, Cr^{3+} *etc.*) when layers bear vacancies (Lanson *et al.*, 2000; Lanson, Drits, Feng & Manceau, 2002, Lanson, Drits, Gaillot *et al.*, 2002; Manceau *et al.*, 2002; Webb *et al.*, 2005; Peacock & Sherman, 2007*a*,*b*; Peña *et al.*, 2010; Sherman & Peacock, 2010). Vernadite reactivity is reinforced by its nanocrystallinity which is responsible for a high density of pH-dependent sorption sites at layer edges (Appelo & Postma, 1999; Tonkin *et al.*, 2004; Rihs *et al.*, 2014) compared with basal sites. As a result, vernadite controls the fate of many elements among trace metals and rare-earth elements in a variety of preserved areas such as soils and rivers (*e.g.* Liu *et al.*, 2002; Hochella *et al.*, 2005). In these environments, pH may span over a wide range of values, depending on rock substratum, presence of organic acids (Jones, 1998) and activity of living forms (*e.g.* Springett, 1983; Haimi & Huhta, 1990). Soil pH may also depend on seasonal cycles (Frankland *et al.*, 1963; Farley & Fitter, 1999). As pH-dependent structural evolution of phyllomanganates was reported for synthetic birnessite (Silvester *et al.*, 1997; Lanson *et al.*, 2000; Lanson, Drits, Gaillot *et al.*, 2002; Manceau *et al.*, 2002), the potential dependence of vernadite structure on pH has to be understood to assess its influence on the geochemical cycles of elements. At pH 10, birnessite layers are almost vacancy-free and contain $\sim 1/3$ Mn^{3+} and $\sim 2/3$ Mn^{4+}. Layer charge is mainly compensated for by interlayer Na^{+}. The structural formula is $Na^{+}_{0.30}(Mn^{4+}_{0.74}Mn^{3+}_{0.21}Mn^{2+}_{0.05})O_{\sim 2}\cdot nH_2O$, where species within brackets are layer cations, and those to the left are interlayer species. Mn^{3+} is a Jahn–Teller ion with two apical O atoms at a distance significantly larger than the four equatorial ones in octahedral coordination (Töpfer *et al.*, 1995; Rodriguez-Carvajal *et al.*, 1998). To minimize layer strains, distorted Mn^{3+} octahedra are segregated in rows parallel to the **b** axis, thus degrading layer symmetry from hexagonal to orthogonal ($a > b \times 3^{1/2}$) and leading to an overall triclinic space group (Lanson, Drits, Feng & Manceau, 2002). When equilibrated at lower pH values, major structural evolutions affect triclinic birnessite. First, H^{+} replace about one third of interlayer Na^{+} as the charge-compensating species, and the same amount of layer Mn^{3+} disproportionate into Mn^{4+} and Mn^{2+}, the latter migrating to the interlayer and being slowly sorbed above/below newly formed vacancies depending on solution pH. The remaining Na^{+} is then progressively replaced by H^{+} after migration of about half of the remaining layer Mn^{3+} above/below newly formed vacancies. Depending on solution pH, additional Mn^{3+} cations originating from partial birnessite dissolution may also readsorb above/below layer vacancies. At pH 3, the birnessite structural formula is $H^{+}_{0.33}Mn^{3+}_{0.143}Mn^{2+}_{0.023}(Mn^{4+}_{0.722}Mn^{3+}_{0.111}Vac_{0.167})O_2(OH)^{-}_{0.033}\cdot 0.467H_2O$, with 'Vac' representing 'layer vacancy' (Lanson *et al.*, 2000). The creation of layer vacancies, which bear a formal charge of four electrons, enhances the affinity of the low-pH birnessite variety for multivalent trace elements such as trace metals.

In addition to such a pH-dependent structural evolution, vernadite may undergo a layer-to-tunnel structure transformation. Vernadite transformation into todorokite (a tectomanganate with 3×3 tunnel size) or cryptomelane (2×2 tunnel structure) has been observed in aqueous suspensions of synthetic precursors (Luo *et al.*, 1999; Al-Attar & Dyer, 2002; Cui *et al.*, 2009, 2010; Zhang *et al.*, 2011), but also in the environment where vernadite is often associated with todorokite. From direct observations of the topotactic transformation, Bodeï *et al.* (2007) concluded that todorokite can form from a magnesium-rich vernadite precursor. However, such an observation is still lacking in ambient air conditions and thus questions the origin of tectomanganates found in surface soils (Taylor *et al.*, 1964; Glasby & Hodgson, 1971; Ross *et al.*, 1976; McKenzie, 1989). Such a structural evolution would also have a significant impact on the fate of trace elements as phyllomanganates can sorb cations both as outer- and inner-sphere complexes on both lateral and basal surfaces, whereas tectomanganates can sorb ions only as an outer-sphere complex and possess a much lower specific surface area than that of phyllomanganates. Mn octahedra at the edges of todorokite triple chains are large enough, however, to accommodate cations larger than Mn^{4+} (*e.g.* Mg^{2+} or Ni^{2+}; Post & Bish, 1988; Post *et al.*, 2003). It is thus likely that cations sorbed at layer vacancies in the initial layer structure can be incorporated in the resulting tunnel structure during phyllomanganate-to-tectomanganate transformation (Bodeï *et al.*, 2007). As a consequence, this transformation could be a sink for a number of elements.

In an effort to better understand the structural stability of phyllomanganate nanoparticles in the environment, the present study combines chemical characterization, thermogravimetric analysis coupled with differential scanning calorimetry and simulation of powder X-ray diffraction data. As a result the structure of δ-MnO_2 equilibrated at pH ranging from 3 to 10 was determined together with its evolution in ambient air over a period of 8 years.

2. Materials and methods

2.1. Sample preparation and chemical analyses

δ-MnO_2 was synthesized following the redox method reported by Villalobos *et al.* (2003, 2006). In a final step, different aliquots were equilibrated at target pH by dropwise addition of HCl. Equilibration times varied as a function of the final pH but never exceeded 12 h. Samples are labelled MndBiXX, where XX stands for the equilibration pH. Following their initial characterization, MndBiXX samples were aged in the dry state for up to 8 years in closed polystyrene containers kept in the dark. Aged samples are labelled

MndBiXX_Zy, where Z stands for the ageing time (4 or 8 years). MndBi7 and MndBi8 could not be aged, as they were fully consumed during measurements of fresh samples, whereas MndBi6 could only be aged for four years for similar reasons.

Total Na and Mn contents were analysed by inductively coupled plasma-atomic emission spectrometry (ICP-AES, Perkin–Elmer Optima 3000) after dissolution of ~ 5 mg of sample in ~ 15 ml of NH_3OHCl (0.7 mol L^{-1}). Mean manganese oxidation degree was obtained by potentiometric titration, using $(NH_4)_2Fe(SO_4)$ (Mohr salt) and sodium pyrophosphate (Lingane & Karplus, 1946; Vetter & Jaeger, 1966). Thermal analyses were performed using a Simultan Thermal Analyzer STA 409EP (Netzsch Instruments). Thermogravimetric analyses (TGA) and differential scanning calorimetry (DSC) were simultaneously monitored on 10–15 mg samples heated up to 673 K at 0.1 K s^{-1}.

2.2. Powder X-ray diffraction data collection and simulation

X-ray diffraction (XRD) patterns of fresh samples and of those aged for 4 years were collected over the 5–80° 2θ interval using a Bruker D5000 diffractometer, equipped with a SolX solid-state detector from Baltic Scientific Instruments and Cu $K\alpha$ radiation (λ = 1.5418 Å). Counting time was 40 s per 0.04° 2θ angular step. XRD patterns of samples aged for 8 years were collected using the same experimental conditions and a Bruker D8 Advance diffractometer, equipped with a SolXE detector from Baltic Scientific Instruments. XRD patterns of turbostratic structures exhibit only unresolved *hk* diffraction bands and 00*l* Bragg peaks (Warren, 1941; Brindley & Brown, 1980; Giovanoli, 1980). A specific trial-and-error method (Drits & Tchoubar, 1990; Drits *et al.*, 1998; Plançon, 2002) was thus used for XRD pattern simulation. This approach, whose robustness was assessed by quantitative comparison with results obtained using the pair distribution function (Manceau *et al.*, 2013), was successfully applied to the determination of turbostratic phyllosilicates, phyllomanganates and nanocrystalline calcium silicate hydrate structures (Chukhrov *et al.*, 1985; Manceau *et al.*, 1997, 2000; Drits *et al.*, 1998; Villalobos *et al.*, 2006; Lanson *et al.*, 2008; Grangeon, Claret, Lerouge *et al.*, 2013; Grangeon, Claret, Linard & Chiaberge, 2013). This method prevents however the calculation of a covariance matrix and thus the estimation of uncertainties. To overcome this limitation, tests have been performed to assess the sensitivity of diffracted intensity to layer symmetry, coherent scattering domain (CSD) size (*i.e.* crystallite size) both in the **ab** plane and along the **c*** axis (*i.e.* the number of layers stacked parallel to each other), lattice parameters or atomic position and site occupancy (Manceau *et al.*, 1997; Villalobos *et al.*, 2006; Drits *et al.*, 2007; Grangeon *et al.*, 2008, 2010; Lanson *et al.*, 2008). Sensitivity to the composition of the interlayer space and to lattice parameters was also observed by Lafferty *et al.* (2010) and Yin *et al.* (2012, 2013).

All atomic positions within the unit cell except those of interlayer H_2O molecules (O atoms) were taken from previous studies (Grangeon *et al.*, 2008, 2012) to reduce the number of refined parameters. The interlayer composition, namely abundance of sodium, trivalent manganese and H_2O molecules, was constrained by chemical analyses after total dissolution, potentiometric titrations [assuming that Mn is fully trivalent in the interlayer, following Grangeon *et al.* (2008) and stoichiometric considerations discussed below], and thermo-gravimetric analyses, respectively. Refined parameters were thus limited to the position of interlayer H_2O molecules in the **ab** plane, *b* and *c** unit-cell parameters ($a = b \times 3^{1/2}$), the CSD sizes in the **ab** plane and along the **c*** axis, and site occupancies (except for layer oxygen, whose occupancy was constrained to 1). The quality of the simulations was

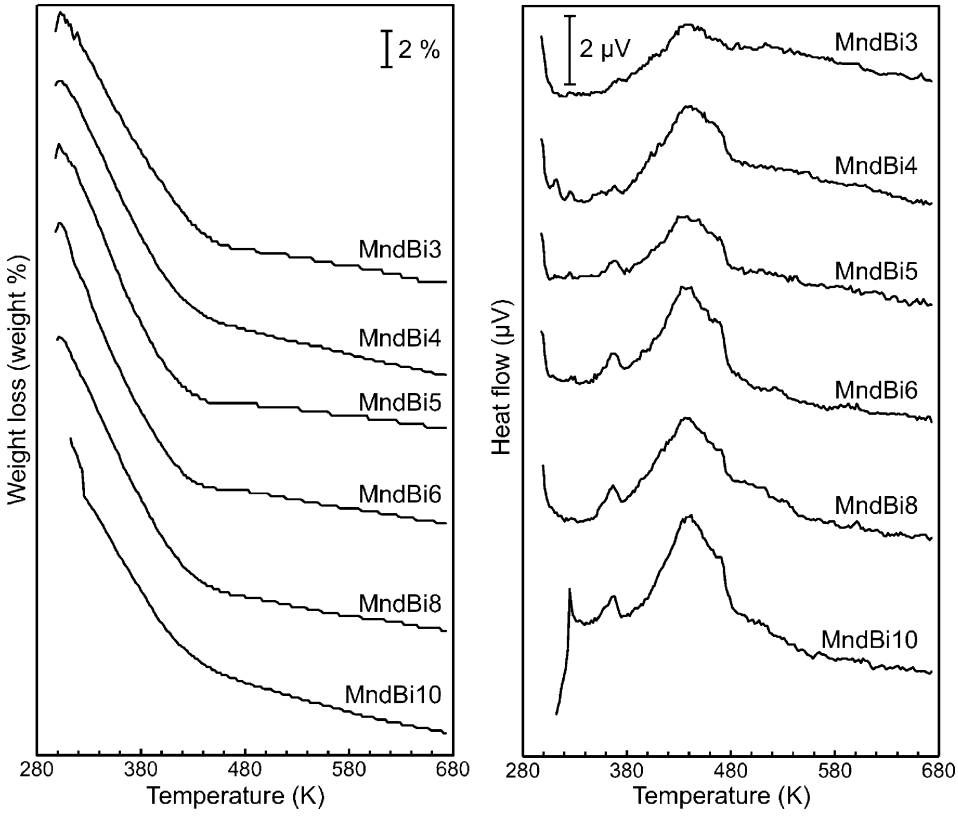

Figure 1
Experimental (*a*) TG and (*b*) DSC curves obtained for MndBi3, MndBi4, MndBi5, MndBi6, MndBi8 and MndBi10 (from top to bottom).

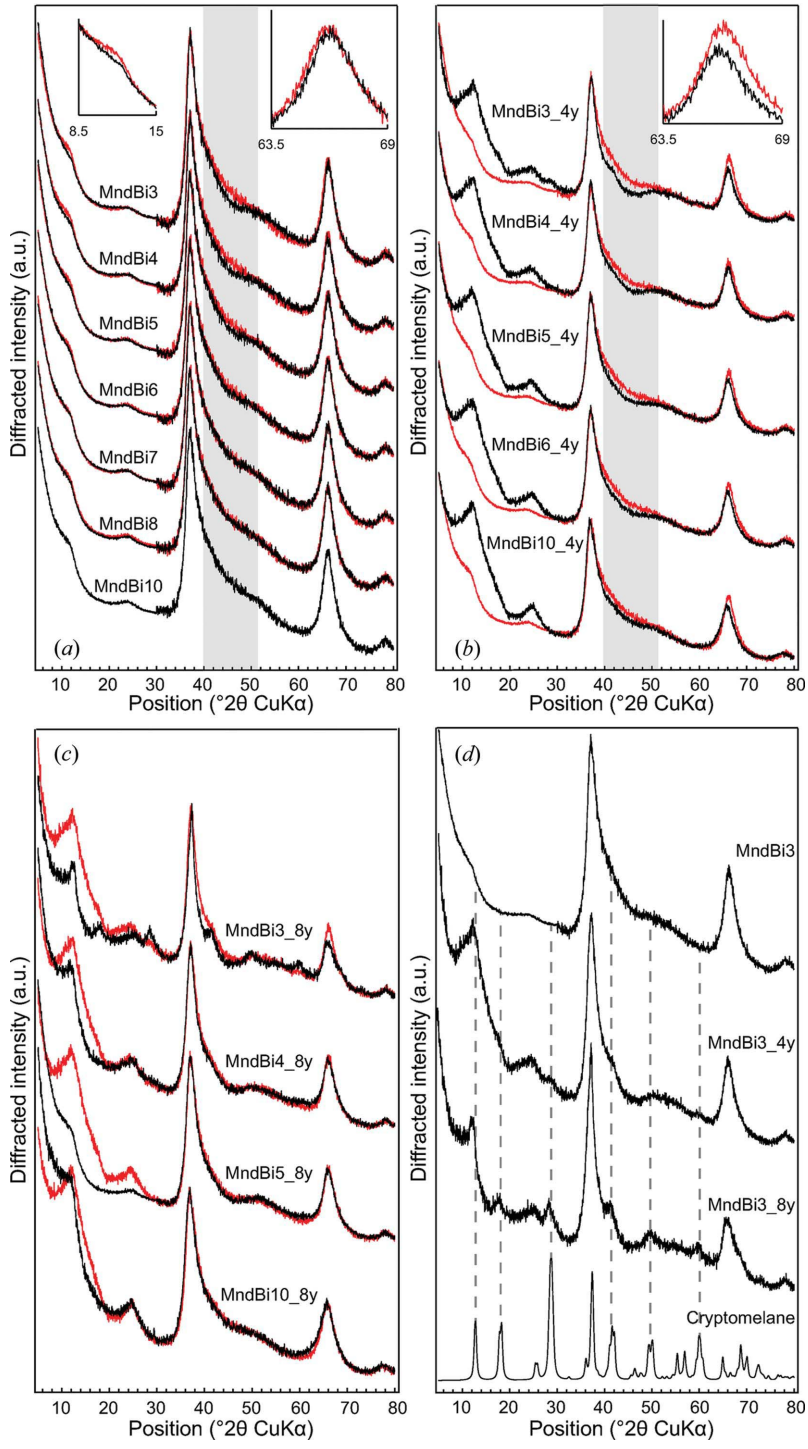

Figure 2
Experimental powder XRD patterns obtained for fresh and aged MndBi samples. (*a*) XRD patterns obtained for MndBi3, MndBi4, MndBi5, MndBi6, MndBi7, MndBi8 and MndBi10 (from top to bottom). Experimental patterns (solid black lines) are plotted over MndBi10 pattern (solid red line) to emphasize the evolution of the XRD traces with pH. Intensity scale factor 5 over the 30–80° 2θ Cu $K\alpha$ range compared with the low-angle region. The gray area highlights the angular range most sensitive to the number of interlayer species at TC sites. Insets: Zoom over the 001 reflection (left) and the [31,02] diffraction band (right) when comparing MndBi3 (solid black line) and MndBi10 (solid red line). (*b*) XRD patterns obtained for MndBi3_4y, MndBi4_4y, MndBi5_4y, MndBi6_4y and MndBi10_4y (from top to bottom). Experimental patterns (solid black lines) are plotted over MndBi3, MndBi4, MndBi5, MndBi6 and MndBi10 patterns, respectively (solid red line), to emphasize the evolution of XRD traces with time. Intensity scale as in (*a*) for fresh samples and uniform for aged samples. The gray area as in (*a*). Inset: Zoom over the [31,02] diffraction band when comparing MndBi3_4y and MndBi10_4y (solid black and red lines, respectively). (*c*) XRD patterns obtained for MndBi3_8y, MndBi4_8y, MndBi5_8y and MndBi10_8y (from top to bottom) are plotted as solid black lines over MndBi3_4y, MndBi4_4y, MndBi5_4y and MndBi10_4y (solid red lines). Intensity scale uniform for all samples but MndBi5_8y (intensity factor 3 over the 30–80° 2θ range). (*d*) XRD patterns obtained for MndBi3, MndBi3_4y and MndBi3_8y, and calculated for cryptomelane structure (from top to bottom). Dotted lines indicate the positions of the main cryptomelane peaks.

Table 1
Chemical composition of δ-MnO_2.

Inter. H_2O and Mn. ox. deg. represent for interlayer water and mean manganese oxidation degree. Layer Mn^{3+}, expressed as site occupancy per layer octahedron, is calculated from Mn. ox. deg. and the number of interlayer Mn deduced from XRD profile modelling.

Sample	Na/Mn (at. %)	Inter. H_2O (wt %)	Mn. ox. deg.	Layer Mn^{3+}
MndBi3	6.99 ± 0.16	5.44 ± 0.5	3.70 ± 0.01	0.12 ± 0.02
MndBi4	11.02 ± 0.13	5.84 ± 0.5	3.72 ± 0.02	0.13 ± 0.02
MndBi5	15.73 ± 0.12	5.88 ± 0.5	3.73 ± 0.01	0.12 ± 0.02
MndBi6	17.39 ± 0.13	5.62 ± 0.5	3.73 ± 0.01	0.14 ± 0.02
MndBi7	19.75 ± 0.09	N.d.	3.74 ± 0.01	0.14 ± 0.02
MndBi8	23.44 ± 0.14	6.04 ± 0.5	3.78 ± 0.01	0.10 ± 0.02
MndBi10	27.66 ± 0.20	5.60 ± 0.5	3.80 ± 0.01	0.10 ± 0.02

evaluated with the usual R_{wp} and goodness-of-fit (GoF = R^2_{wp}/R^2_{exp}) factors (Howard & Preston, 1989).

3. Results

3.1. Chemical characterization of the fresh material

As pH decreases, both Na/Mn ratio and mean Mn oxidation degree decrease (Table 1), similar to the evolution reported for Ni-sorbed δ-MnO_2 (pH 7 to pH 4; Grangeon *et al.*, 2008) and Zn-sorbed δ-MnO_2 (pH 7 to pH 5; Grangeon *et al.*, 2012). A similar dependence of the mean Mn oxidation degree on pH was also reported for synthetic samples (Zhao *et al.*, 2009) and for uncharacterized manganese oxides from natural soils (Negra *et al.*, 2005). In all the present samples the mean manganese oxidation degree is close to 4, consistent with Mn^{4+} prevalence, and reaches the highest values for high-pH samples, suggesting an increasing proportion of Mn^{3+} with decreasing pH.

DSC data exhibit two exothermic peaks ending at ∼ 373 and 478 K (Fig. 1) assigned to non-structural water sorbed on crystal external surfaces and to interlayer water, respectively, according to previous gravimetric studies (Giovanoli, 1994). The amount of interlayer water (H_2O) was thus calculated from the weight loss between 373 and 478 K, although weight loss is almost linear over the 323–473 K range, possibly owing to an overlap in the losses of sorbed and interlayer water. This simultaneity is likely related to the nanocrystallinity of δ-MnO_2: as crystals are typically built up of less than three layers (*e.g.* Villalobos *et al.*, 2003; Grangeon *et al.*, 2008; Lanson *et al.*, 2008), a large part of 'interlayer' water is exposed on external surfaces. This hypothesis is supported by data from Giovanoli (1994) who reported a smoother inflection point at ∼ 373 K in TG curves for vernadite compared with well ordered Na phyllomanganate. The resulting contents of interlayer H_2O may thus be slightly underestimated, but relative values in different samples hold true, as H_2O loss curves are essentially parallel to each other below 473 K (Fig. 1). Finally, exothermic peaks on DSC curves are more pronounced for samples equilibrated at high pH than for those equilibrated at low pH. This behaviour remains unexplained for the 373 K peak, whereas the broadening of the 478 K peak may be related to lower CSD sizes along the **c*** axis in low-pH samples, thus increasing the proportion of 'interlayer water' exposed at crystal surfaces.

Table 2
Crystal data.

Notes: $\gamma = 90°$. The CSD size in the **ab** plane is expressed as the mean diameter of disk-shaped domains.

	Unit-cell parameters			Average CSD size (nm)	
Sample	*a* (Å)	*b* (Å)	*c** (Å)	In the **ab** plane	Along **c***
MndBi3	4.909	2.834	7.2	6.0	1.0
MndBi4	4.910	2.835	7.2	6.6	1.1
MndBi5	4.914	2.837	7.2	6.7	1.1
MndBi6	4.916	2.838	7.2	6.7	1.1
MndBi7	4.917	2.839	7.2	6.0	1.2
MndBi8	4.919	2.840	7.2	7.0	1.2
MndBi10	4.922	2.842	7.2	7.0	1.2
MndBi4_4y	4.910	2.835	N.d.†	6.8	N.d.†
MndBi5_4y	4.919	2.840	N.d.†	7.0	N.d.†
MndBi6_4y	4.919	2.840	N.d.†	7.0	N.d.†
MndBi10_4y	4.938	2.851	N.d.†	7.6	N.d.†
MndBi4_8y	N.d.‡	N.d.‡	7.2	N.d.‡	2.1
MndBi5_8y	N.d.‡	N.d.‡	7.2	N.d.‡	1.7
MndBi10_8y	N.d.‡	N.d.‡	7.2	N.d.‡	1.7

† 00*l* reflections could not be simulated because of their high-angle asymmetry (see text for details). ‡ Not determined, XRD patterns similar to those recorded on samples aged for 4 years.

3.2. Qualitative description of XRD patterns from fresh material

XRD patterns are typical for nanocrystalline turbostratic phyllomanganates (Fig. 2*a*) with a few diffraction maxima that can be indexed with a C-centred unit cell, as proposed previously (*e.g.* Drits *et al.*, 2007). Diffraction maxima at ∼ 12.0° 2θ (7.4 Å) and ∼ 24.7° 2θ (3.6 Å) are attributed to [001] and [002] reflections although they do not form a rational series owing to the minute CSD size (Drits & Tchoubar, 1990). Peaks at ∼ 37.3° 2θ (2.41 Å), ∼ 66.3° 2θ (1.41 Å) and ∼ 78.4° 2θ (1.22 Å) correspond to the [11,20], [31,02] and [22,40] diffraction bands, respectively. The [31,02]

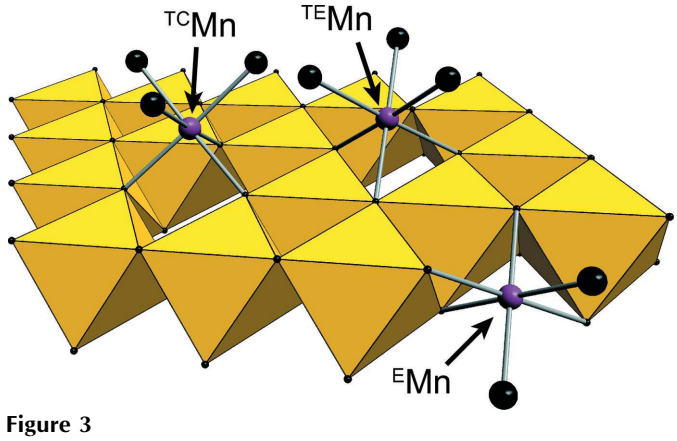

Figure 3
Schematic representation of the different Mn sites (ball-and-sticks) on the δ-MnO_2 surface that were observed in the present study. ^{E}Mn represents the octahedral layer site and ^{TC}Mn and ^{TE}Mn, respectively, are the triple corner-sharing and triple edge-sharing sites. The closed polyhedra schematize layer $(MnO_6)^{8-}$ octahedra.

band is almost symmetrical in all XRD patterns, indicating hexagonal layer symmetry (Drits *et al.*, 2007). With increasing pH, diffraction profiles are significantly modified (Fig. 2*a*): (i) the [001] reflection increases in intensity (Fig. 2*a*, left inset); (ii) the hump on the high-angle side of the [11,20] band becomes ill-defined (Fig. 2*a*, gray area); (iii) the [31,02] band shifts towards higher angles (Fig. 2*a*, right inset). These evolutions indicate: (i) larger CSD sizes along the **c*** axis; (ii) a decreasing number of 'heavy' interlayer cations in triple-corner sharing configuration above and/or below layer vacancies (TC configuration – Fig. 3); (iii) an increase of in-plane unit-cell dimensions. Comparison with XRD patterns of biogenic and synthetic vernadite from the literature (Villalobos *et al.*, 2006; Grangeon *et al.*, 2008, 2010; Lanson *et al.*, 2008) indicates that MndBi10 contains less than 0.1 interlayer cation sorbed at TC sites per layer octahedron, whereas MndBi3 hosts ~ 0.2. No evolution of the hump between ~ 42 and $\sim 46^\circ$ 2θ can be observed when decreasing pH from 10 to 7, thus suggesting either a stable interlayer structure or concomitant changes of different crystallographic parameters compensating each other to a certain extent. This can only be unravelled by XRD pattern modelling.

3.3. Qualitative description of XRD patterns from aged material

XRD patterns of samples aged for 4 years systematically differ from those of fresh samples (Fig. 2*b*). Over the low-angle region, basal reflections of four-year samples are better defined and more intense, which denote an increase of the CSD size along the **c*** axis. Parallel to this improved definition, the high-angle shoulder of the reflection at $\sim 12^\circ$ 2θ Cu $K\alpha$ is significantly increased with a shoulder at 17–18° 2θ Cu $K\alpha$ visible for a few samples. A second difference is visible over the 27–47° 2θ Cu $K\alpha$ range, where the minimum at $\sim 46^\circ$ 2θ Cu $K\alpha$ is systematically better defined in XRD patterns from aged samples. In addition, a shoulder at $\sim 42^\circ$ 2θ Cu $K\alpha$ is observed in XRD patterns from MndBi3_4y and MndBi4_4y. Both features indicate an increasing number of heavy interlayer species at TC sites, as such a shoulder was observed only in samples hosting 0.3 ^{TC}Mn or more per layer octahedron (Grangeon *et al.*, 2010). A third difference lies in the position of the [31,20] band which is generally shifted towards higher *d* values in aged samples, compared with fresh ones, denoting an increase of the *a* and *b* unit-cell parameters. Finally,

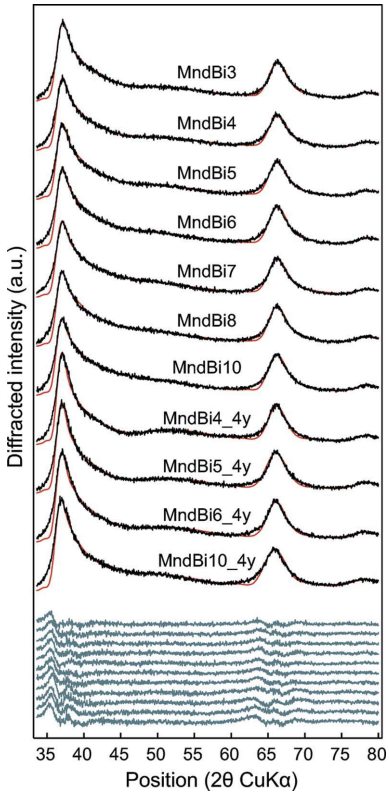

Figure 4
Comparison between experimental and calculated (*hk* bands only) XRD patterns for MndBi3, MndBi4, MndBi5, MndBi6, MndBi7, MndBi8, MndBi10, MndBi4_4y, MndBi5_4y, MndBi6_4y and MndBi10_4y (from top to bottom). Experimental and calculated patterns are shown as solid black and red lines, respectively. Difference plots are shown as solid gray lines at the bottom of the figure. R_{wp} factors are respectively 0.057, 0.068, 0.063, 0.072, 0.066, 0.068, 0.072, 0.069, 0.062, 0.069 and 0.071, and GoF factors are 3.66, 4.77, 4.41, 5.58, 4.93, 5.10, 5.99, 6.10, 4.94, 6.19 and 6.69.

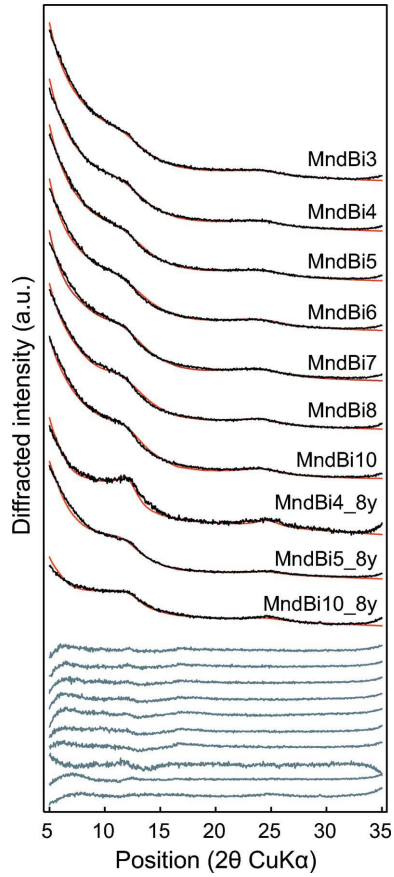

Figure 5
Comparison between experimental and calculated (00*l* reflections only) XRD patterns for MndBi3, MndBi4, MndBi5, MndBi6, MndBi7, MndBi8, MndBi10, MndBi4_8y, MndBi5_8y and MndBi10_8y (from top to bottom). Patterns as for Fig. 3. R_{wp} factors are, respectively, 0.035, 0.033, 0.032, 0.035, 0.045, 0.037, 0.048, 0.042, 0.016 and 0.045 and GoF factors are 4.07, 3.77, 3.66, 5.58, 4.93, 4.66, 8.07, 4.13, 1.10 and 5.19.

Table 3
Atomic coordinates and site occupancies of δ-MnO_2.

Notes: the *C*2/*m* space group may be used to represent the structure model. However, equivalent positions from adjacent layers must not be generated, as δ-MnO_2 has no periodicity along **c***. Occupancies are given per octahedral layer site (*i.e.* per half unit cell) and as the sum of (x, y, z) and $(-x, -y, -z)$ sites. Debye–Waller factors were fixed to 0.5 Å^2 for Mn1, 1 Å^2 for O1, Mn2 and Mn3, and 2 Å^2 for all other atoms. The different Mn layer and interlayer sites are schematized in Fig. 3.

	Coordinates			Site occupancy										
Atom	*x*	*y*	*z*	MndBi3	MndBi4	MndBi5	MndBi6	MndBi7	MndBi8	MndBi10	MndBi4_4y	MndBi5_4y	MndBi6_4y	MndBi10_4y
^{E}Mn (Mn1)	0	0	0	0.830	0.850	0.850	0.850	0.850	0.850	0.860	0.740	0.740	0.770	0.790
O_{Mn1} (O1)	0.333	0	0.139	2.000	2.000	2.000	2.000	2.000	2.000	2.000	2.000	2.000	2.000	2.000
^{TC}Mn (Mn2)	0	0	0.299	0.175	0.150	0.130	0.115	0.100	0.090	0.075	0.300	0.280	0.230	0.165
O_{Mn2} (O2)	−0.333	0	0.472	0.525	0.450	0.390	0.345	0.300	0.270	0.225	0.900	0.840	0.690	0.495
^{TE}Mn (Mn3)	−0.333	0	0.299	0.010	0.010	0.010	0.010	0.015	0.015	0.020	0.015	0.030	0.030	0.040
O_{Mn3} (O3)	0	0	0.472	0.030	0.030	0.030	0.030	0.450	0.045	0.060	0.450	0.090	0.090	0.120
Na^+	−0.525	0	0.500	0.020	0.040	0.050	0.060	0.066	0.080	0.090	0.040	0.050	0.060	0.090
Na^+	−0.238	0.288	0.500	0.020	0.040	0.050	0.060	0.066	0.080	0.090	0.040	0.050	0.060	0.090
Na^+	−0.238	−0.288	0.500	0.020	0.040	0.050	0.060	0.066	0.080	0.090	0.040	0.050	0.060	0.090
O_{Na+} (O4)	0.190	0	0.500	0.100	0.100	0.100	0.100	0.100	0.100	0.100	0.100	0.100	0.100	0.100
O_{Na+} (O4)	−0.095	0.285	0.500	0.100	0.100	0.100	0.100	0.100	0.100	0.100	0.100	0.100	0.100	0.100
O_{Na+} (O4)	−0.095	−0.285	0.500	0.100	0.100	0.100	0.100	0.100	0.100	0.100	0.100	0.100	0.100	0.100

MndBi3_4y exhibits additional weak modulations at ~ 28.5 and $\sim 60.0^\circ$ 2θ Cu $K\alpha$ that are attributable to cryptomelane, a tectomanganate with 2×2 tunnel size.

From 4 to 8 years of ageing, the evolution of XRD patterns is minimal for MndBi4_8y, MndBi5_8y and MndBi10_8y except in the shape of the [001] reflections (Fig. 2*c*), which are sharper and more symmetrical for samples aged for 8 years. Contrastingly, MndBi3_8y significantly differs from MndBi3_4y, with more pronounced diffraction maxima at positions expected for cryptomelane (Fig. 2*d*).

3.4. XRD pattern simulation

Simulations of fresh and aged δ-MnO_2 XRD patterns are presented in Figs. 4 and 5, whereas structural parameters are reported in Tables 2 and 3. MndBi3 interlayer contains, within uncertainties, the same density (0.175 per layer octahedron) of $^{TC}Mn^{3+}$ than that of layer vacancy (0.17), and each vacancy is thus likely capped by ^{TC}Mn on a single side. Chemical analyses and thermogravimetry results constrain the number of H_2O molecules and sodium hosted at the interlayer mid-plane (0.3 and 0.06 per layer octahedron, respectively). With increasing pH, the number of interlayer $^{TC}Mn^{3+}$ decreases, whereas that of interlayer sodium increases (0.075 and 0.27 per layer octahedron at pH 10, respectively), consistent with previous reports (Zhu *et al.*, 2010). The number of layer vacancies slightly decreases (0.14 per layer octahedron at pH 10), whereas the number of interlayer H_2O molecules is constant. In-plane unit-cell parameters and CSD sizes steadily increase, respectively, from b = 2.834 Å (MndBi3) to 2.842 Å (MndBi10), CSD = 6 nm (MndBi3) to 7 nm (MndBi10) in the **ab** plane and from 1.0 nm (MndBi3) to 1.2 nm (MndBi10) along the **c*** axis. XRD pattern simulations successfully accounted for the number of interlayer H_2O molecules and sodium determined by chemical methods. Contrastingly, the mean manganese oxidation degree calculated from the refined numbers of $^{TC}Mn^{3+}$ and layer Mn, the latter being considered as Mn^{4+}, is systematically higher than that measured by chemical titration. The presence of layer Mn^{3+} has thus to be invoked to conceal this apparent inconsistency. The proportion of layer Mn^{3+} does not vary significantly with equilibrium pH, ranging from 0.10 ± 0.02 to 0.14 ± 0.02 per layer octahedron (MndBi10 and MndBi6, respectively; Table 1).

With 0.17–0.15 layer vacancies and 0.12–0.13 layer Mn^{3+} per layer octahedron, low-pH samples (pH = 3–5) are structurally similar to synthetic birnessites (hereafter referred to as HBi), the three-dimensional ordered variety of vernadite that contain 0.17 layer vacancies and 0.11 layer Mn^{3+} independent of pH (pH = 2–5; Lanson *et al.*, 2000). Similarly, HBi hosts 0.166 interlayer ^{TC}Mn, compared with 0.175–0.130 in δ-MnO_2. The structural analogy between turbostratic and three-dimensional-ordered phyllomanganates no longer holds at high pH, especially with the coexistence of layer Mn^{3+} and vacancies (0.10 ± 0.02 and 0.14 per layer octahedron, respectively, at pH 10). δ-MnO_2 thus has hexagonal layer symmetry even at high pH, whereas high-pH birnessite (hereafter referred to as NaBi) layers exhibit orthogonal symmetry ($a > b \times 3^{1/2}$) owing to the cooperative distortion of Mn^{3+} octahedra (Lanson, Drits, Feng & Manceau, 2002; Gaillot *et al.*, 2005). NaBi has indeed 0.21 layer Mn^{3+} and 0.05

layer Mn^{2+} per layer octahedron segregated in rows parallel to the **b** axis and separated from each other by two rows of Mn^{4+} octahedra to minimize steric strains.

For samples initially equilibrated at pH values ranging from 4 to 10, a 4 year ageing leads to a mean increase of their *b* unit-cell parameters by ~ 0.003 Å, hexagonal layer symmetry being preserved (Table 2). The number of both layer vacancies and interlayer ^{TC}Mn also increases by a mean value of 0.09 and 0.14 per layer octahedron, respectively (Table 3), whereas Na/Mn ratios are similar in both fresh and aged samples (microprobe analyses of aged samples – data not shown). Finally, CSD sizes within the **ab** plane increase by 0.2 to 0.6 nm. Basal reflections could not be satisfactorily simulated because of their strong high-angle asymmetry.

No simulation of *hk* bands was attempted for samples aged for 8 years, either because of the cryptomelane contribution (MndBi3_8y) or because of the similarity with 4 year samples (MndBi4_8y, MndBi5_8y, MndBi8_8y). Simulation of basal reflections reveals an average increase of $\sim 50\%$ of the CSD along the **c*** axis compared with fresh samples.

4. Discussion

4.1. Influence of pH on δ-MnO_2 structure

Partial dissolution affects MndBi when pH is decreased from 10 to 3, as attested by the decreasing size of CSD from 7 to 6 nm in the **ab** plane, and from 1.2 to 1.0 nm along the **c*** axis. This releases layer manganese (Mn^{4+} and Mn^{3+}) in solution, which partly re-adsorbs above/below layer vacancies replacing interlayer sodium as a charge compensating species.

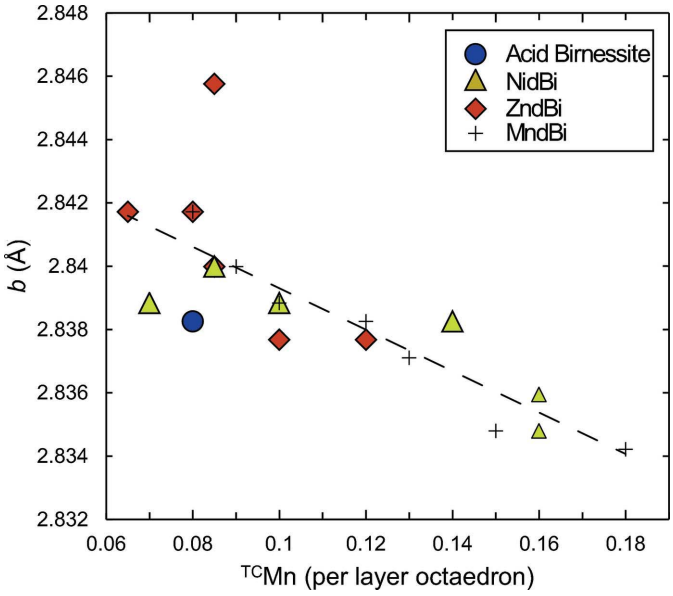

Figure 6
Evolution of the unit-cell parameter *b* in synthetic δ-MnO_2 as a function of the number of Mn^{3+} at TC sites. Acid birnessite (Villalobos *et al.*, 2006), Ni-sorbed δ-MnO_2 (Grangeon *et al.*, 2008), Zn-sorbed δ-MnO_2 (Grangeon *et al.*, 2012) and samples from the present study are shown as circles, triangles, diamonds and crosses, respectively. The dotted line is a linear regression to the data ($r^2 = 0.64$).

Readsorbed Mn cations replace 2.8 Na^+ on average, thus supporting the trivalent oxidation degree of interlayer Mn (Table 3). The minor deviation from electrical neutrality possibly results from a combination of proton adsorption at low pH and of uncertainties on site occupancy. In addition, the number of layer vacancies increases from 0.14 to 0.17 per layer octahedron (in MndBi10 and MndBi3, respectively). Disproportionation of layer Mn^{3+}, that would lead to an increase in layer vacancies and in ^{TC}Mn, as observed in birnessite (Drits *et al.*, 1997), cannot be invoked here owing to the similar number of the former in all fresh samples. Rather, the increased number of layer vacancies is likely also related to partial dissolution at acidic pH, the effect being reinforced compared with synthetic birnessite, owing to the nanocrystallinity of δ-MnO_2. Re-adsorption of Mn at TC sites lowers in turn the mean manganese oxidation degree.

When decreasing pH from 10 to 3, in-plane unit-cell parameters of δ-MnO_2 decrease from $b = 2.842$ to 2.834 Å (MndBi10 and MndBi3, respectively, with $a = b \times 3^{1/2}$). At low pH, these values (2.837, 2.835 and 2.834 Å, at pH 5, 4, and 3, respectively) are lower than those of their micrometric three-dimensional ordered counterparts (HBi: 2.852, 2.848 and 2.845 Å, respectively). The numbers of both layer Mn^{3+} and layer vacancies being similar in HBi and δ-MnO_2, the reduction of unit-cell parameters is most likely related to an increased corrugation or bending of the octahedral layers in δ-MnO_2, as previously deduced using the Debye equation analysis (Manceau *et al.*, 2013). Amongst the structural parameters, the unit-cell parameter *b* of δ-MnO_2 (and therefore *a*) was best correlated with the number of interlayer Mn at TC sites (^{TC}Mn), even when other cations (Zn, Ni) occupy the same site (Fig. 6). As discussed for HBi (Lanson *et al.*, 2000), layer contraction results from the migration towards each other in the **ab** plane of O atoms shared by layer and interlayer Mn to minimize their electrostatic repulsion. The lower valence of Zn^{2+} and Ni^{2+} certainly reduces this effect compared with Mn^{3+}, although it certainly persists (Kwon *et al.*, 2009).

4.2. Mechanisms of structural evolution with time

For all samples whose X-ray diffraction patterns were fitted, the number of both layer vacancies and ^{TC}Mn increases with ageing time. For example, the number of layer vacancies is 0.15 and 0.26 for MndBi4 and MndBi4_4y, respectively, whereas that of ^{TC}Mn also increases from 0.15 to 0.30 per layer octahedron, thus indicating migration of layer Mn above newly formed vacancies. The driving force for such a spontaneous migration being likely the reduction of internal strains, layer Mn^{3+} are most probably concerned owing to the Jahn–Teller distortion of their coordination octahedra. The number of layer vacancies consistently increases on average by 0.09 ± 0.02 per layer octahedron for samples equilibrated between pH 4 and 10, matching the number of layer Mn^{3+} in fresh samples (0.12 ± 0.02 per layer octahedron). From the negative correlation shown in Fig. 6, creation of additional vacant layer sites capped by ^{TC}Mn is expected to result in a

Table 4
Compilation of literature data on the phyllomanganate to tectomanganate transformation.

Note: buserite and birnessite are 10 and 7 Å phyllomanganates, respectively. δ-MnO_2 is a turbostratic birnessite.

Starting sample	Interlayer cation	Synthesis conditions	Resulting tunnel size	Reference
Synthetic birnessite	Mg	Autoclaving at 428 K for 8 h	[3 × 3]	Golden *et al.* (1986)
Synthetic buserite	Cu, Ni, Co, Zn, Mg, Ca, Sr, Ba, Li, K, Rb, Cs	413 K for 20 min	[3 × 3] for Cu, Nu, Co, Zn, Mg [2 × 2] for Ca, Sr, Ba, Li, K, Rb, Cs	Luo *et al.* (1999)
Synthetic buserite	All alkali but Fr, all first-row transition metals, Pb, Ag, all lanthanides but Sc, Tm, Yb, Al, Sn	Hydrothermal treatment	[3 × 3] for all ions but La, Ba, Ce and Cr	Luo *et al.* (1999)
Synthetic buserite and synthetic birnessite	Li	423 K for 2 d	[2 × 2] in the case of birnessite [3 × 3] in the case of buserite	Luo *et al.* (1999)
Synthetic buserite	Ca, Mg, Ni, Na, Li, K, Cs, Ba, Cu, Co, Zn	Autoclaving for 8 h at 428 K	[2 × 2] and [3 × 3] for samples with 7 and 10 Å initial basal distances, respectively	Al-Attar & Dyer (2002)
Synthetic birnessite	Mg	Reflux	[3 × 3]	Feng *et al.* (2004)
Natural (probably vernadite)	Mg	Natural sample (topotactic transformation)	[3 × 3]	Bodeï *et al.* (2007)
Synthetic buserite	Cu	Reflux	[3 × 3]	Cui *et al.* (2009)
Synthetic buserite	Mg	12 h at 353 K and then ageing (up to 1 year)	[3 × 3]	Cui *et al.* (2010)
Biogenic δ-MnO_2	Mg	Reflux	[3 × 3]	Feng *et al.* (2010)
δ-MnO_2	K	Reflux and ageing	[2 × 2]	Zhang *et al.* (2011)

reduction of unit-cell parameters *a* and *b*, whereas the opposite is observed (for MndBi10, parameter *b* increases from 2.842 to 2.851 Å after 4 years of ageing). Consistent with the previous discussion, unit-cell expansion is possibly related to a reduced degree of layer bending, thus improving parallelism between adjacent layers, or to a reduced layer corrugation, as a consequence of the lower number of Jahn–Teller distorted Mn^{3+} octahedra within the layers. Both phenomena would lead to a higher CSD size in the **ab** plane, as observed here. In addition, it is likely that Mn octahedra at the edges of chains have larger Mn—O distances, as reported for todorokite (Post & Bish, 1988), thus contributing to unit-cell expansion during the phyllomanganate transformation. Further ageing of samples initially equilibrated at pH 4 to 8 does not result in additional structure modifications most likely because samples aged for 4 years no longer contain layer Mn^{3+}. The observed absence of evolution indicates that layer-to-interlayer migration of Mn^{3+} is the main driving force for structural evolution.

In addition to the above-described evolution, MndBi3_4y exhibits weak diffraction maxima of cryptomelane that precluded profile fitting. With the number of layer Mn^{3+} being similar (within errors), in MndBi3 and MndBi4 it is logical to hypothesize similar increases of ^{TC}Mn in both samples after 4 years of ageing. As a result, MndBi3_4y would contain $\sim 0.175 + 0.15 = 0.325$ ^{TC}Mn per layer octahedron, close to the highest possible value of 0.333. At this value, neighbouring ^{TC}Mn, within a unique layer or from adjacent layers, must be distributed as far as possible from each other to avoid sharing coordination oxygens. For ^{TC}Mn from adjacent layers, such a rule of avoidance would require ordered layer stacking (as every displacement from the optimal position, in the layer plane, would reduce the distance between neighbouring ^{TC}Mn from adjacent layers), which is not fulfilled for δ-MnO_2. Turbostratism implies systematic random stacking faults between successive layers and, in turn, the implicit sharing of coordination O atoms by ^{TC}Mn from adjacent layers and the creation of local tunnel-like fragments (Fig. 7). The increase of cryptomelane contribution observed from MndBi3_4y to MndBi3_8y is consistent with an increased sharing of coordination spheres by ^{TC}Mn from adjacent layers that would result from a solid-state rearrangement of adjacent layers.

Tectomanganate formation from 7 and 10 Å phyllomanganate precursors has been widely reported in the literature, both in natural samples and under hydrothermal conditions (Table 4). The tunnel size of newly formed tectomanganates is most frequently [3 × 3] (todorokite), but [2 × 2] tunnel sizes (cryptomelane), as in the present study, have also been reported. Todorokite appears to form when the initial phyllomanganate has a 10 Å layer-to-layer distance and when the interlayer cation is not an alkali. Alkali cations form outer-sphere complexes in phyllomanganate interlayers and are unable to form

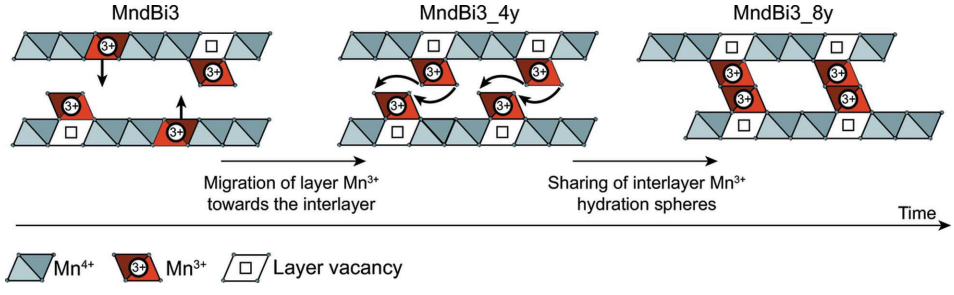

Figure 7
Proposed mechanism for the structural evolution of δ-MnO_2 with time.

the $M(OH)_2$ template (M being the interlayer cation) that is likely to be necessary for the formation of tectomanganate 'walls' (Cui *et al.*, 2010). The transformation of δ-MnO_2 into cryptomelane in aqueous solution is complete after 24 h for solution pH ranging from 0.83 to 2.26, whereas reaction completion is only partial at pH 5.60 and no reaction occurs at pH from 7.14 to 8.05 (Zhang *et al.*, 2011). Consistent with the present work, the complete transformation to cryptomelane at pH values of 2 and below is likely due to an increased number of $^{TC}Mn^{3+}$ acting as a template ion for the tunnel 'walls'.

References

Al-Attar, L. & Dyer, A. (2002). *J. Mater. Chem.* **12**, 1381–1386.
Appelo, C. & Postma, D. (1999). *Geochim. Cosmochim. Acta*, **63**, 3039–3048.
Bodeï, S., Manceau, A., Geoffroy, N., Baronnet, A. & Buatier, M. (2007). *Geochim. Cosmochim. Acta*, **71**, 5698–5716.
Brindley, G. W. & Brown, G. (1980). Editors. *Crystal Structures of Clay Minerals and their X-ray Identification*, pp. 125–195. London: Mineralogical Society.
Chukhrov, F. V., Sakharov, B. A., Gorshkov, A. I., Drits, V. A. & Dikov, Y. P. (1985). *Int. Geol. Rev.* **27**, 1082–1088.
Cui, H., Feng, X., Tan, W., He, J., Hu, R. & Liu, F. (2009). *Microporous Mesoporous Mater.* **117**, 41–47.
Cui, H., Liu, F., Feng, X., Tan, W. & Wang, M. K. (2010). *J. Soils Sediments*, **10**, 1540–1547.
Drits, V. A., Lanson, B. & Gaillot, A. (2007). *Am. Mineral.* **92**, 771–788.
Drits, V. A., Lanson, B., Gorshkov, A. I. & Manceau, A. (1998). *Am. Mineral.* **83**, 97–118.
Drits, V. A., Silvester, E., Gorshkov, A. I. & Manceau, A. (1997). *Am. Mineral.* **82**, 946–961.
Drits, V. A. & Tchoubar, C. (1990). Editors. *X-ray Diffraction by Disordered Lamellar Structures: Theory and Applications to Microdivided Silicates and Carbons.* Berlin: Springer-Verlag.
Farley, R. A. & Fitter, A. H. (1999). *J. Ecol.* **87**, 688–696.
Feng, X. H., Tan, W. F., Liu, F., Wang, J. B. & Ruan, H. D. (2004). *Chem. Mater.* **16**, 4330–4336.
Feng, X. H., Zhu, M., Ginder-Vogel, M., Ni, C., Parikh, S. J. & Sparks, D. L. (2010). *Geochim. Cosmochim. Acta*, **74**, 3232–3245.
Frankland, J. C., Ovington, J. D. & Macrae, C. (1963). *J. Ecol.* **51**, 97–112.
Gaillot, A., Lanson, B. & Drits, V. A. (2005). *Chem. Mater.* **17**, 2959–2975.
Giovanoli, R. (1980). *Mineralium Deposita*, **15**, 251–253.
Giovanoli, R. (1994). *Thermochim. Acta*, **234**, 303–313.
Glasby, G. P. & Hodgson, G. W. (1971). *Geochim. Cosmochim. Acta*, **35**, 845–851.
Golden, D. C., Chen, C. C. & Dixon, J. B. (1986). *Science*, **231**, 717–719.
Grangeon, S., Claret, F., Lerouge, C., Warmont, F., Sato, T., Anraku, S., Numako, C., Linard, Y. & Lanson, B. (2013). *Cem. Concr. Res.* **52**, 31–37.
Grangeon, S., Claret, F., Linard, Y. & Chiaberge, C. (2013). *Acta Cryst.* B**69**, 465–473.
Grangeon, S., Lanson, B., Lanson, M. & Manceau, A. (2008). *Mineral. Mag.* **72**, 1197–1209.
Grangeon, S., Lanson, B., Miyata, N., Tani, Y. & Manceau, A. (2010). *Am. Mineral.* **95**, 1608–1616.
Grangeon, S., Manceau, A., Guilhermet, J., Gaillot, A., Lanson, M. & Lanson, B. (2012). *Geochim. Cosmochim. Acta*, **85**, 302–313.
Haimi, J. & Huhta, V. (1990). *Biol. Fertil. Soils*, **10**, 178–183.
Hochella, M. F. Jr, Kasama, T., Putnis, A., Putnis, C. V. & Moore, J. N. (2005). *Am. Mineral.* **90**, 718–724.
Howard, S. A. & Preston, K. D. (1989). *Rev. Mineral. Geochem.* **20**, 217–275.
Jones, D. L. (1998). *Plant Soil*, **205**, 25–44.
Kwon, K. D., Refson, K. & Sposito, G. (2009). *Geochim. Cosmochim. Acta*, **73**, 1273–1284.
Lafferty, B. J., Ginder-Vogel, M., Zhu, M., Livi, K. J. & Sparks, D. L. (2010). *Environ. Sci. Technol.* **44**, 8467–8472.
Lanson, B., Drits, V. A., Feng, Q. & Manceau, A. (2002). *Am. Mineral.* **87**, 1662–1671.
Lanson, B., Drits, V. A., Gaillot, A.-C., Silvester, E., Plancon, A. & Manceau, A. (2002). *Am. Mineral.* **87**, 1631–1645.
Lanson, B., Drits, V. A., Silvester, E. & Manceau, A. (2000). *Am. Mineral.* **85**, 826–838.
Lanson, B., Marcus, M. A., Fakra, S., Panfili, F., Geoffroy, N. & Manceau, A. (2008). *Geochim. Cosmochim. Acta*, **72**, 2478–2490.
Lingane, J. J. & Karplus, R. (1946). *Ind. Eng. Chem. Anal. Ed.* **18**, 191–194.
Liu, F., Colombo, C., Adamo, P., He, J. Z. & Violante, A. (2002). *Soil Sci. Soc. Am. J.* **66**, 661–670.
Luo, J., Zhang, Q., Huang, A., Giraldo, O. & Suib, S. L. (1999). *Inorg. Chem.* **38**, 6106–6113.
Manceau, A., Drits, V. A., Silvester, E., Bartoli, C. & Lanson, B. (1997). *Am. Mineral.* **82**, 1150–1175.
Manceau, A., Lanson, B. & Drits, V. A. (2002). *Geochim. Cosmochim. Acta*, **66**, 2639–2663.
Manceau, A., Lanson, B., Drits, V. A., Chateigner, D., Gates, W. P., Wu, J., Huo, D. & Stucki, J. W. (2000). *Am. Mineral.* **85**, 133–152.
Manceau, A., Marcus, M. A., Grangeon, S., Lanson, M., Lanson, B., Gaillot, A.-C., Skanthakumar, S. & Soderholm, L. (2013). *J. Appl. Cryst.* **46**, 193–209.
McKenzie, R. M. (1989). *Minerals in Soil Environments*, edited by J. B. Dixon & S. B. Weed, pp. 439–461. Madison: Soil Science Society of America.
Negra, C., Ross, D. S. & Lanzirotti, A. (2005). *Soil Sci. Soc. Am. J.* **69**, 87–95.
Peacock, C. L. & Sherman, D. M. (2007*a*). *Am. Mineral.* **92**, 1087–1092.
Peacock, C. L. & Sherman, D. M. (2007*b*). *Chem. Geol.* **238**, 94–106.
Peña, J., Kwon, K. D., Refson, K., Bargar, J. R. & Sposito, G. (2010). *Geochim. Cosmochim. Acta*, **74**, 3076–3089.
Plançon, A. (2002). *J. Appl. Cryst.* **35**, 377.
Post, J. E. & Bish, D. L. (1988). *Am. Mineral.* **73**, 861–869.
Post, J. E., Heaney, P. J. & Hanson, J. (2003). *Am. Mineral.* **88**, 142–150.
Rihs, S., Gaillard, C., Reich, T. & Kohler, S. J. (2014). *Chem. Geol.* **373**, 59–70.
Rodriguez-Carvajal, J., Hennion, M., Moussa, F. & Moudden, A. H. (1998). *Phys. Rev. B*, **57**, R3189–R3192.
Ross, S. J., Franzmeier, D. P. & Roth, C. B. (1976). *Soil Sci. Soc. Am. J.* **40**, 137–143.
Sherman, D. M. & Peacock, C. L. (2010). *Geochim. Cosmochim. Acta*, **74**, 6721–6730.
Silvester, E., Manceau, A. & Drits, V. A. (1997). *Am. Mineral.* **82**, 962–978.
Springett, J. A. (1983). *J. Appl. Ecol.* **20**, 865–872.
Taylor, R., McKenzie, R. & Norrish, K. (1964). *Aust. J. Soil Res.* **2**, 235–248.
Tonkin, J. W., Balistrieri, L. S. & Murray, J. W. (2004). *Appl. Geochem.* **19**, 29–53.
Töpfer, J., Trari, M., Gravereau, P., Chaminade, J. P. & Doumerc, J. P. (1995). *Z. Kristallogr.* **210**, 184–187.
Vetter, K. J. & Jaeger, N. (1966). *Electrochim. Acta*, **11**, 401–419.
Villalobos, M., Lanson, B., Manceau, A., Toner, B. & Sposito, G. (2006). *Am. Mineral.* **91**, 489–502.
Villalobos, M., Toner, B., Bargar, J. & Sposito, G. (2003). *Geochim. Cosmochim. Acta*, **67**, 2649–2662.
Warren, B. E. (1941). *Phys. Rev.* **59**, 693–698.

Webb, S. M., Tebo, B. M. & Barger, J. R. (2005). *Geomicrobiol. J.* **22**, 181–193.
Yin, H., Liu, F., Feng, X., Hu, T., Zheng, L., Qiu, G., Koopal, L. K. & Tan, W. (2013). *Geochim. Cosmochim. Acta*, **117**, 1–15.
Yin, H., Tan, W., Zheng, L., Cui, H., Qiu, G., Liu, F. & Feng, X. (2012). *Geochim. Cosmochim. Acta*, **93**, 47–62.
Zhang, Q., Xiao, Z., Feng, X., Tan, W., Qiu, G. & Liu, F. (2011). *Mater. Chem. Phys.* **125**, 678–685.
Zhao, W., Cui, H., Liu, F., Tan, W. & Feng, X. (2009). *Clays Clay Miner.* **57**, 513–520.
Zhu, M., Ginder-Vogel, M., Parikh, S. J., Feng, X. H. & Sparks, D. L. (2010). *Environ. Sci. Technol.* **44**, 4465–4471.